CrossMark

One Planet or Two Planets? The Ultra-sensitive Extreme-magnification Microlensing Event KMT-2019-BLG-1953

Cheongho Han[1,25] , Doeon Kim[1], Youn Kil Jung[2,25], Andrew Gould[3,4,25], Ian A. Bond[5,26]
(Leading authors),
Michael D. Albrow[6] , Sun-Ju Chung[2,7] , Kyu-Ha Hwang[2], Chung-Uk Lee[2], Yoon-Hyun Ryu[2] , In-Gu Shin[2] ,
Yossi Shvartzvald[8] , Jennifer C. Yee[9] , Weicheng Zang[10] , Sang-Mok Cha[2,11], Dong-Jin Kim[2], Hyoun-Woo Kim[2],
Seung-Lee Kim[2,7], Dong-Joo Lee[2], Yongseok Lee[2,11], Byeong-Gon Park[2,7], Richard W. Pogge[4] , Woong-Tae Kim[12]
(The KMTNet Collaboration),
and
Fumio Abe[13], Richard Barry[14] , David P. Bennett[14,15] , Aparna Bhattacharya[14,15], Martin Donachie[16], Hirosane Fujii[13],
Akihiko Fukui[17,18] , Yoshitaka Itow[13] , Yuki Hirao[19], Rintaro Kirikawa[19], Iona Kondo[19], Naoki Koshimoto[20,21] ,
Man Cheung Alex Li[16], Yutaka Matsubara[13], Yasushi Muraki[13], Shota Miyazaki[19] , Masayuki Nagakane[19], Clément Ranc[14] ,
Nicholas J. Rattenbury[16] , Yuki Satoh[19], Hikaru Shoji[19], Haruno Suematsu[19], Takahiro Sumi[19], Daisuke Suzuki[22] ,
Yuzuru Tanaka[19], Paul J. Tristram[23], Tsubasa Yamawaki[19], and Atsunori Yonehara[24]
(The MOA Collaboration)

[1] Department of Physics, Chungbuk National University, Cheongju 28644, Republic of Korea; cheongho@astroph.chungbuk.ac.kr
[2] Korea Astronomy and Space Science Institute, Daejon 34055, Republic of Korea
[3] Max Planck Institute for Astronomy, Königstuhl 17, D-69117 Heidelberg, Germany
[4] Department of Astronomy, Ohio State University, 140 W. 18th Ave., Columbus, OH 43210, USA
[5] Institute of Natural and Mathematical Sciences, Massey University, Auckland 0745, New Zealand
[6] University of Canterbury, Department of Physics and Astronomy, Private Bag 4800, Christchurch 8020, New Zealand
[7] Korea University of Science and Technology, 217 Gajeong-ro, Yuseong-gu, Daejeon, 34113, Republic of Korea
[8] Department of Particle Physics and Astrophysics, Weizmann Institute of Science, Rehovot 76100, Israel
[9] Center for Astrophysics|Harvard & Smithsonian 60 Garden St., Cambridge, MA 02138, USA
[10] Department of Astronomy and Tsinghua Centre for Astrophysics, Tsinghua University, Beijing 100084, People's Republic of China
[11] School of Space Research, Kyung Hee University, Yongin, Kyeonggi 17104, Republic of Korea
[12] Department of Physics & Astronomy, Seoul National University, Seoul 08826, Republic of Korea
[13] Institute for Space-Earth Environmental Research, Nagoya University, Nagoya 464-8601, Japan
[14] Code 667, NASA Goddard Space Flight Center, Greenbelt, MD 20771, USA
[15] Department of Astronomy, University of Maryland, College Park, MD 20742, USA
[16] Department of Physics, University of Auckland, Private Bag 92019, Auckland, New Zealand
[17] Instituto de Astrofísica de Canarias, Vía Láctea s/n, E-38205 La Laguna, Tenerife, Spain
[18] Department of Earth and Planetary Science, Graduate School of Science, The University of Tokyo, 7-3-1 Hongo, Bunkyo-ku, Tokyo 113-0033, Japan
[19] Department of Earth and Space Science, Graduate School of Science, Osaka University, Toyonaka, Osaka 560-0043, Japan
[20] Department of Astronomy, Graduate School of Science, The University of Tokyo, 7-3-1 Hongo, Bunkyo-ku, Tokyo 113-0033, Japan
[21] National Astronomical Observatory of Japan, 2-21-1 Osawa, Mitaka, Tokyo 181-8588, Japan
[22] Institute of Space and Astronautical Science, Japan Aerospace Exploration Agency, 3-1-1 Yoshinodai, Chuo, Sagamihara, Kanagawa, 252-5210, Japan
[23] University of Canterbury Mt. John Observatory, P.O. Box 56, Lake Tekapo 8770, New Zealand
[24] Department of Physics, Faculty of Science, Kyoto Sangyo University, 603-8555 Kyoto, Japan

Abstract

We present the analysis of a very high-magnification ($A \sim 900$) microlensing event KMT-2019-BLG-1953. A single-lens single-source (1L1S) model appears to approximately delineate the observed light curve, but the residuals from the model exhibit small but obvious deviations in the peak region. A binary-lens (2L1S) model with a mass ratio of $q \sim 2 \times 10^{-3}$ improves the fits by $\Delta\chi^2 = 181.8$, indicating that the lens possesses a planetary companion. From additional modeling by introducing an extra planetary lens component (3L1S model) and an extra source companion (2L2S model), it is found that the residuals from the 2L1S model further diminish, but claiming these interpretations is difficult due to the weak signals with $\Delta\chi^2 = 16.0$ and 13.5 for the 3L1S and 2L2L models, respectively. From a Bayesian analysis, we estimate that the host of the planets has a mass of $M_{\rm host} = 0.31^{+0.37}_{-0.17} \, M_\odot$ and that the planetary system is located at a distance of $D_{\rm L} = 7.04^{+1.10}_{-1.33}$ kpc toward the Galactic center. The mass of the securely detected planet is $M_{\rm p} = 0.64^{+0.76}_{-0.35} \, M_{\rm J}$. The signal of the potential second planet could have been confirmed if the peak of the light curve had been more densely observed by follow-up observations, and thus the event illustrates the need for intensive follow-up observations for very high-magnification events even in the current generation of high-cadence surveys.

Unified Astronomy Thesaurus concepts: Gravitational microlensing (672); Gravitational microlensing exoplanet detection (2147)

---

[25] KMTNet Collaboration.
[26] MOA Collaboration.

1. Introduction

Microlensing events with very high magnifications are of scientific importance for various reasons. First, the chance for the lens to pass over the surface of the source star is high for these events, and this allows one to measure the angular Einstein radius θ_E, from which the physical parameters of the lens can be better constrained (Gould 1994b; Nemiroff & Wickramasinghe 1994; Witt & Mao 1994). Second, the detection probability is very high for planets located in the lensing zone of the host, and thus high-magnification events provide an efficient channel to detect microlensing planets (Griest & Safizadeh 1998).

Another scientific importance of high-magnification events is that they provide a channel to detect multiplanetary systems. The basis for this use of microlensing lies in the properties of lensing caustics induced by planets. A planet located in the vicinity of the Einstein ring induces two sets of caustics, in which one is located away from the host of the planet (planetary caustic) and the other is located close to the host (central caustic). See Han (2006) and Chung et al. (2005) for the properties of the planetary and central caustics, respectively. If a lens has multiple planets, the individual planets induce central caustics in the common central magnification region and affect the magnification pattern of the region. For very high-magnification events, that are produced by the source passage through the central magnification region, then, the chance to detect the signatures of the individual planets is high (Gaudi et al. 1998).

The usefulness of the high-magnification channel in detecting multiplanetary systems has been demonstrated by the fact that three out of four known microlensing multiplanetary systems were detected through this channel. The first multiplanetary system detected through this channel is OGLE-2006-BLG-109L, in which two planets with masses of $\sim 0.71\,M_J$ and $\sim 0.27\,M_J$ are orbiting around a primary star of a mass $\sim 0.50\,M_\odot$ with projected orbital separations of ~ 2.3 and ~ 4.6 au (Gaudi et al. 2008; Bennett et al. 2016). This system resembles a scaled version of our solar system in that the mass ratio, separation ratio, and equilibrium temperatures of the planets are similar to those of Jupiter and Saturn of the solar system. The microlens OGLE-2012-BLG-0026L is the second system, in which the lens consists of two planets with masses of $\sim 0.14\,M_J$ and $\sim 0.86\,M_J$ and projected separations of ~ 4.0 and ~ 4.8 au from the host with about a solar mass (Han et al. 2013; Beaulieu et al. 2016). The third system is OGLE-2018-BLG-101L, which is composed of two planets with masses $\sim 1.8\,M_J$ and $\sim 2.8\,M_J$ around a host with a mass of $\sim 0.18\,M_\odot$. The system is located at a distance of ~ 7.1 kpc and it is the farthest system among the known multiplanetary systems (Han et al. 2019). Besides these microlensing multiplanetary systems, Ryu et al. (2020) pointed out the possibility that the lens of the lensing event OGLE-2018-BLG-0532 might have a second planet although there also existed another interpretation of the signal. The multiplanetary system OGLE-2014-BLG-1722L (Suzuki et al. 2018) was detected from the planetary signals produced by the combination of the planetary and central caustics.

In this paper, we present the analysis of a very high-magnification lensing event KMT-2019-BLG-1953. For the presentation of the analysis, we organize the paper as follows. In Section 2, we describe the observations of the event and the data used in the analysis. In Section 3, we present analysis of the data conducted under various interpretations of the event.

We estimate the angular Einstein radius in Section 4 and estimate the physical lens parameters in Section 5. In Section 6, we discuss the importance of follow-up observations for extreme lensing events for both planet detections and physical lens parameter determinations. In Section 7, we summarize the results of the analysis and conclude.

2. Observation and Data

The lensing event KMT-2019-BLG-1953 occurred on a star located toward the Galactic bulge field. The equatorial coordinates of the lensed star (source) are $(\mathrm{R.A., decl.})_{J2000} = (17\!:\!56\!:\!27.90, -28\!:\!12\!:\!04.00)$. The corresponding Galactic coordinates are $(l, b) = (1°85, -1°67)$.

The magnification of the source flux induced by lensing was first found by the Korea Microlensing Telescope Network (KMTNet) survey (Kim et al. 2016, 2018) on 2019 August 5 $(\mathrm{HJD}' \equiv \mathrm{HJD} - 2,450,000 \sim 8701)$ when the magnification of the source flux was $A \sim 13$. The KMTNet survey was conducted utilizing three identical 1.6 m telescopes that were globally located at the Siding Spring Observatory in Australia (KMTA), Cerro Tololo Interamerican Observatory in Chile (KMTC), and the South African Astronomical Observatory in South Africa (KMTS). Each of the KMTNet telescopes was equipped with a camera consisting of four $9k \times 9k$ chips, yielding a $4\,\mathrm{deg}^2$ field of view. Images from the survey were mainly taken in the I band and a subset of images were obtained in the V band for the source color measurements. The event was located in the two overlapping KMTNet fields of BLG02 and BLG42, toward which observations were conducted most frequently among the total 27 KMTNet fields. Being located in the two overlapping fields in which each field was observed with a 30 minutes cadence, the event was observed with a combined cadence of 15 minutes. The cadence of the V-band observations was about one-tenth of the I-band cadence.

Photometry of the data was conducted using the pipeline developed by Albrow et al. (2009) based on the difference imaging method (Tomaney & Crotts 1996; Alard & Lupton 1998). For the source color measurement, additional photometry was conducted using the pyDIA code (Albrow 2017) for a subset of the KMTA data set. For the data used in the analysis, error bars from the photometry pipelines were readjusted following the routine described in Yee et al. (2012).

We note that there exist additional data of the event acquired by the Microlensing Observations in Astrophysics (MOA; Bond et al. 2001) survey. The MOA survey found the event, designated as MOA 2019-BLG-372, two days after the detection by the KMTNet survey. The MOA data are not used in the analysis because (1) the observational cadence is low, (2) the peak of the light curve is not covered, and (3) the photometric quality of the data is not high.

In Figure 1, we present the light curve of the lensing event. It shows that the source flux is greatly magnified. From modeling the light curve based on a single-source and single-lens (1L1S) interpretation, it is found that the source flux is magnified by $A_{\mathrm{peak}} \sim 900$ at the peak. We will discuss the modeling in the following section. Figure 2 shows the zoomed-in view around the peak region of the light curve, which shows the deviation affected by finite-source effects. The duration of the finite-source deviation was about 2 hr.
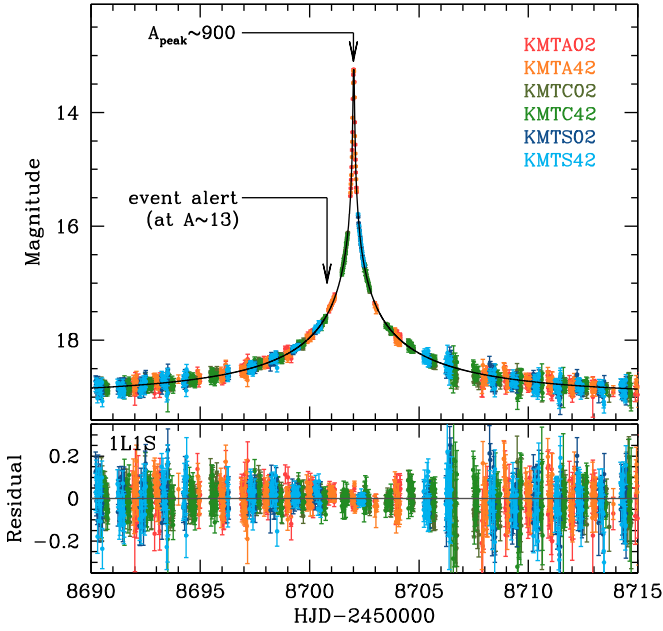
Figure 1. Light curve of KMT-2019-BLG-1953. The curve superposed on the data points is the model based on a 1L1S interpretation considering finite-source effects and the lower panel shows the residual from the model. Telescopes used to acquire the data are marked in the legend, and the colors of the individual telescopes and data points are chosen to match one another.

3. Modeling Light Curve

3.1. 1L1S Modeling

Considering the apparently smooth and symmetric shape, we first model the observed light curve with a 1L1S interpretation. Modeling is carried out by searching for the lensing parameters that best describe the observed light curve. A 1L1S lensing light curve affected by finite-source effects is described by four lensing parameters. These parameters include t_0, u_0, t_E, and ρ, which represent the time of the closest lens-source approach, the lens-source separation at that time (impact parameter), the event timescale, and the normalized source radius, respectively. The lensing parameters are searched for using a downhill approach based on the MCMC method. In computing finite-source magnifications, we use the semi-analytic expression that was derived by Gould (1994a) and later expanded by Yoo et al. (2004) to consider the variation of the source star's surface brightness caused by limb darkening. We choose the limb-darkening coefficients from the table of Claret (2000) based on the source type. The procedure for determining the source type will be discussed in Section 4.

In Table 1, we present the best-fit lensing parameters of the 1L1S model. To be noted among the lensing parameters is that the impact parameter of the lens-source approach, $u_0 = (0.70 \pm 0.04) \times 10^{-3}$, is extremely small, resulting in a very high lensing magnification. In Figure 2, we present the 1L1S model curve (dotted curve in the top panel) in the peak region of the light curve. The residuals from the model are shown in the bottom panel. The 1L1S model appears to approximately delineate the observed light curve, but a close inspection of the residuals reveals that the model exhibits small but obvious deviations with $\Delta I \lesssim 0.07$ mag in the peak region. From an additional modeling considering *annual* microlens parallax effects (Gould 1992), it is found that the microlens parallax π_E cannot be measured, mainly due to the relatively
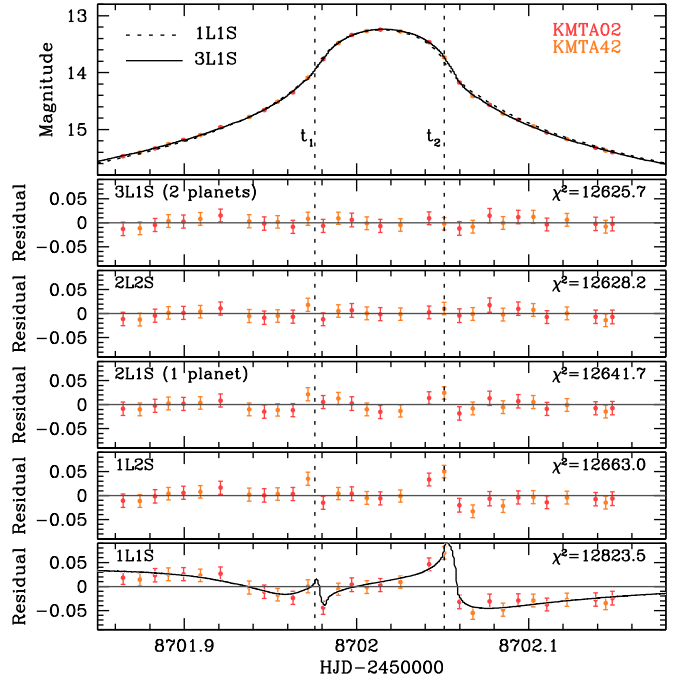
Figure 2. Zoomed-in view around the peak region of the light curve (top panel). Plotted over the data points are the model curves of the 3L1S (solid curve) and 1L1S (dotted curve) solutions. In the five bottom panels, we present the residuals from the five tested models based on the 3L1S, 2L2S, 2L1S, 1L2S, and 1L1S interpretations and mark the χ^2 value of the fits. The two times marked by $t_1 = 8701.975$ and $t_2 = 8702.051$ correspond to the two epochs at which the two caustic-involved bumps in the residuals from the 1L1S model arise. The curve in the bottom panel represents the difference between the 3L1S and 1L1S models.

short timescale, $t_E \sim 16$ days, of the event. It is known that *terrestrial* parallax effects can be detected for events with extreme magnifications (Gould 1997; Gould et al. 2009), and thus we also check the model considering these effects. From this, we find that π_E cannot be securely measured mainly because the peak of the light curve is covered by only a single observatory, i.e., KMTA.

3.2. 2L1S Modeling

Considering that a companion to a lens can induce deviations in the peak region of a very high-magnification event, we check whether the deviation from the 1L1S model can be explained by the existence of a binary companion to the lens. In order to check this possibility, we additionally conduct binary-lens (2L1S) modeling. Adding one more lens component in a lensing modeling requires including additional lensing parameters. These parameters are the projected separation between the lens components, s (normalized to θ_E), the mass ratio between the lens components, $q = M_2/M_1$, and the source trajectory angle as measured from the binary axis, α (source trajectory angle). In the 2L1S modeling, we divide the lensing parameters into two groups. The grid parameters s and q in the first group are searched for using a grid search approach, while the remaining parameters are searched for using a downhill approach based on the MCMC method. In the first-round modeling, we construct $\Delta\chi^2$ maps in the grid-parameter space and investigate the maps to check the existence of local minima that result in possible degenerate solutions. In the second-round modeling, we refine the individual local minima by allowing s

Table 1
Lensing Parameters of the 1L1S, 2L1S, 1L2S, and 2L2S Models

| Parameter	1L1S	2L1S	1L2S	2L2S
χ^2/dof	12823.5/12621	12641.7/12618	12663.0/12617	12628.2/12614
t_0 (HJD′)	8702.015 ± 0.001	8702.016 ± 0.001	8702.015 ± 0.001	8702.014 ± 0.001
$t_{0,2}$ (HJD′)	...	...	8701.949 ± 0.012	8702.042 ± 0.010
u_0 (10^{-3})	0.70 ± 0.04	0.72 ± 0.04	0.02 ± 0.12	0.71 ± 0.06
$u_{0,2}$ (10^{-3})	...	...	7.49 ± 1.16	1.10 ± 0.90
t_{E} (days)	16.60 ± 0.25	16.05 ± 0.23	15.98 ± 0.27	16.01 ± 0.25
s	...	2.51 ± 0.31	...	2.08 ± 0.25
q (10^{-3})	...	1.97 ± 0.63	...	1.37 ± 0.61
α (rad)	...	2.408 ± 0.038	...	2.494 ± 0.028
ρ (10^{-3})	2.32 ± 0.04	2.37 ± 0.04	2.31 ± 0.04	2.33 ± 0.05
ρ_2 (10^{-3})	...	...	7.87 ± 2.93	0.65 ± 0.33
q_F	...	...	0.108 ± 0.009	0.079 ± 0.024

Note. HJD′ ≡ HJD–2,450,000.

and q parameters to vary and find a global solution by comparing the χ^2 values of the local solutions.

We find that the 2L1S model substantially reduces the 1L1S residuals. In Table 1, we present the best-fit lensing parameters of the 2L1S model together with χ^2/dof. Here "dof" denotes the degree of freedom. The measured mass ratio between the binary-lens components is $q \sim 2 \times 10^{-3}$, indicating that the companion to the lens is a planetary-mass object. The 2L1S solution is subject to the well-known close/wide degeneracy (Griest & Safizadeh 1998; Dominik 1999; An 2005). The presence of the degenerate solutions is shown in the $\Delta\chi^2$ map on the s–q plane, shown in Figure 3, constructed from the first-round grid search for solutions. The map shows that there are two locals with $s < 1.0$ (close solution) and $s > 1.0$ (wide solution). The presented parameters in Table 1 are for the solution with $s > 1.0$, and the solution with $s < 1.0$ has similar parameters except $s_{\mathrm{close}} \sim s_{\mathrm{wide}}^{-1}$. In Figure 2, we present the residuals from the 2L1S solution with $s > 1.0$. The 2L1S model improves the fit by $\Delta\chi^2 = 181.8$, indicating that the planet is firmly detected. From the inspection of the residuals, however, it is found that the 2L1S residuals still exhibit subtle deviations from the model. This hints that the 2L1S solution may not be adequate to fully explain the central deviation.

3.3. 1L2S and 2L2S Modeling

We also check the possibility that the source is a binary (2S). We first test a model in which the lens is a single object and the source is a binary: the 1L2S model. Similar to the 2L1S case, a 1L2S modeling requires extra lensing parameters in addition to those of a 1L1S modeling. Following the parameterization of Hwang et al. (2013), these additional parameters are $t_{0,2}$, $u_{0,2}$, ρ_2, and q_F, which represent the time of the closest lens approach to the source companion, the lens–companion separation at $t_{0,2}$, the normalized radius of the companion source star, and the flux ratio between the two source stars, respectively. In the first-round modeling, we set the initial parameters related to the first source (t_0, u_0, t_{E}, and ρ) as those determined from the 1L1S model and test various trajectories of the second source. In the second round, we refine the solutions by letting all parameters vary. The best-fit lensing parameters of the 1L2S solution are presented in Table 1 and the residuals from the solution are shown in Figure 2. It is found that the 1L2S solution improves the fit by $\Delta\chi^2 = 160.5$
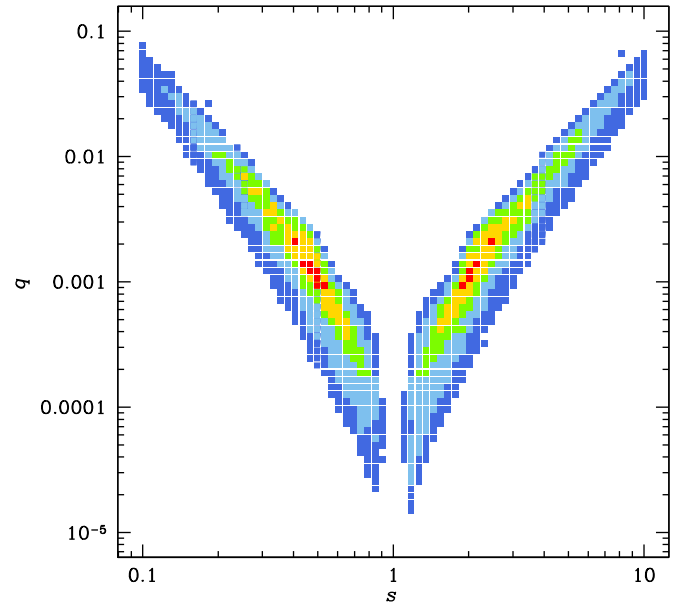

Figure 3. Map of $\Delta\chi^2$ on the s–q parameter plane obtained from the grid searches for the parameters based on the 2L1S modeling. Points with different colors denote the regions with $<1n\sigma$ (red), $<2n\sigma$ (yellow), $<3n\sigma$ (green), $<4n\sigma$ (cyan), and $<5n\sigma$ (blue), where $n = 2$.

with respect to the 1L1S solution, but the fit is worse than the 2L1S solution by $\Delta\chi^2 = 21.3$.

We additionally check a model in which both the lens and source are binaries: the 2L2S model. Considering that the 2L1S solution substantially improves the fit, we start modeling with the initial binary-lens parameters, i.e., (s, q, α), as those of the 2L1S solution. Considering also that the subtle residuals from the 2L1S solution are confined to the peak region of the light curve, we test various source trajectories passing close to the first source. In Figure 2, we present the residuals of the 2L2S solution, and we list the lensing parameters in Table 1. We note that the model is subject to the close/wide degeneracy in s and the presented parameters are for the wide solution with $s > 1.0$. In the lower panel of Figure 4, we present the lens system configuration, in which the source trajectories of the two source stars with respect to the caustic in the central magnification region are shown. It is found that the 2L2S model further reduces the residuals from the 2L1S model. The improvement of the fit is $\Delta\chi^2 = 13.5$ relative to the 2L1S model.
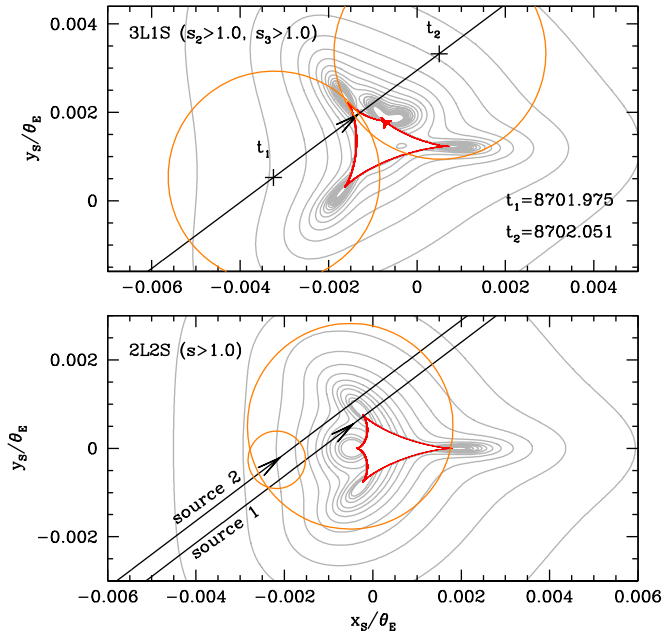
Figure 4. Lens system configurations of the 3L1S (upper panel) and 2L2S (lower panel) models. In each panel, the red cuspy figure represents the caustic, and the line with an arrow denotes the source trajectory. For the 2L2S model, there are two source trajectories corresponding to the individual source stars. The two orange circles in the upper panel represent the source positions at the two epochs marked by t_1 and t_2 in the light curve presented in Figure 2. The orange circles in the lower panel represent the positions of two source stars at t_0. The size of the source circle is scaled to the caustic size. Lengths are scaled to the angular Einstein radius corresponding to the total mass of the lens. The gray curves around the caustic represent equi-magnification contours.

3.4. 3L1S Modeling

Finally, we test a 3L1S model, in which the lens is composed of two planets and their host. We test this model because if an additional planet exists, its signal would appear in the central magnification region, and this may explain the residuals from the 2L1S model. The addition of a third body, M_3, to the binary-lens components, M_1 and M_2, requires three additional lensing parameters in lens modeling. These parameters are the projected separation, s_3, and mass ratio, q_3, between M_1 and M_3, and the orientation angle of M_3 with respect to the M_1–M_2 axis, ψ. To designate the M_1–M_2 separation and M_2/M_1 mass ratio, we use the notations s_2 and q_2, respectively. The subscript "1" is used to designate the host of the planets, and the subscripts "2" and "3" are used to denote the planets. We note that the subscript "2" is used to designate the planet inducing a larger perturbation in the central magnification region. Because a lower-mass planet located close to the Einstein ring of the host can induce a larger perturbation than the perturbation induced by a heavier-mass planet located away from the Einstein ring, the order of the subscripts "2" and "3" are not necessarily arranged by the mass.

In the 3L1S modeling, we start with the lensing parameters (s_2, q_2, α) of the 2L1S solution and search for the parameters related to M_3, i.e., (s_3, q_3, ψ). This strategy is based on the fact that an anomaly induced by two planets, in many cases, is dominated by a single planet and the second planet acts as a perturber (Bozza 1999; Han et al. 2001; Han et al. 2020). Following this strategy, we first conduct grid searches for (s_3, q_3, ψ) parameters by fixing (s_2, q_2, α) parameters and then identify local minima in the parameter planes. Figure 5 shows
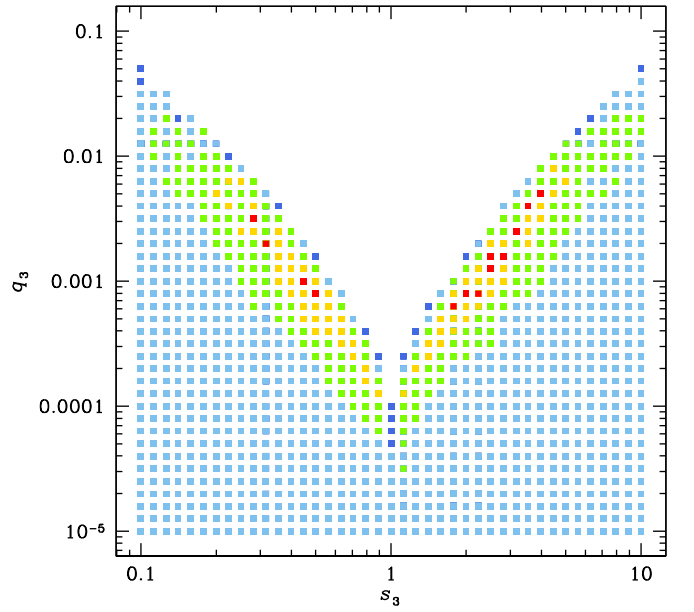
Figure 5. $\Delta\chi^2$ map on the s_3–q_3 plane obtained from the grid search for these parameters based on the 3L1S modeling. The grid search is conducted with the initial values of (s_2, q_2) of the close 2L1S solution. Color coding of the points is same as in Figure 3 except that $n = 1$.

the $\Delta\chi^2$ map on the s_3–q_3 plane constructed from this grid searches using the initial values of (s_2, q_2, α) of the wide 2L1S solution (with $s_2 > 1.0$). In the second round, we refine the individual local solutions by allowing all parameters, including (s_2, q_2, α), to vary.

From the 3L1S modeling, we find four sets of degenerate solutions. The multiplicity of the solutions is caused by the close/wide degeneracies in both s_2 and s_3, and thus the individual solutions have s_2–s_3 pairs of $(s_2 < 1.0, s_3 < 1.0)$ (close–close solution), $(s_2 < 1.0, s_3 > 1.0)$ (close–wide solution), $(s_2 > 1.0, s_3 < 1.0)$ (wide–close solution), and $(s_2 > 1.0, s_3 > 1.0)$ (wide–wide solution), respectively. See the $\Delta\chi^2$ map in Figure 5 showing the two locals on the s_3–q_3 plane with common values of (s_2, q_2). Although the wide–wide solution provides the best fit, the degeneracies among the solutions are severe with $\Delta\chi^2 \leqslant 2.8$. The lensing parameters of the individual solutions are presented in Table 2. The mass ratio of M_3 to M_1 is in the planetary-mass regime regardless of the solutions, with $q_3 \sim (0.8–1.5) \times 10^{-3}$ and $(6.5–8.7) \times 10^{-3}$ for the solutions with $s_3 < 1.0$ and $s_3 > 1.0$, respectively. According to the 3L1S solution, then, the lens is a planetary system with two planets. In the four panels of Figure 6, we present the lens system configurations of the four degenerate 3L1S solutions. In each panel, the positions of the lens components are marked by filled dots and the inset shows the zoomed-in view of the central caustic.

It is found that the 3L1S model further reduces the residuals from the 2L1S solution, improving the fit by $\Delta\chi^2 = 16.0$ with respect to the 2L1S model. In Figure 2, we plot the model curve of the 3L1S wide–wide solution (solid curve in the top panel) and the residuals from the model. The residuals show that the model curve passes through the error bars of all data points around the peak, indicating that the model well describes the observed light curve. To show how the 3L1S model explains the residuals from the 1L1S model, we draw the curve of the difference between the 3L1S and 1L1S solutions in the bottom

Table 2
Lensing Parameters of the 3L1S Model

Parameter	Close–Close $(s_2 < 1.0, s_3 < 1)$	Close–Wide $(s_2 < 1.0, s_3 > 1)$	Wide–Close $(s_2 > 1.0, s_3 < 1)$	Wide–Wide $(s_2 > 1.0, s_3 > 1)$
χ^2/dof	12628.5/12525	12626.6/12525	12627.9/12525	12625.7/12525
t_0 (HJD′)	8702.015 ± 0.002	8702.014 ± 0.002	8702.015 ± 0.001	8702.012 ± 0.001
u_0 (10^{-3})	1.04 ± 0.24	2.17 ± 0.15	1.22 ± 0.09	2.36 ± 0.25
t_E (days)	16.02 ± 0.26	16.08 ± 0.26	16.18 ± 0.25	16.18 ± 0.24
s_2	0.41 ± 0.10	0.47 ± 0.07	2.12 ± 0.13	2.30 ± 0.36
q_2 (10^{-3})	1.82 ± 1.92	1.32 ± 1.30	1.28 ± 0.17	1.91 ± 0.92
α (rad)	2.433 ± 0.070	2.496 ± 0.035	2.456 ± 0.043	2.500 ± 0.029
s_3	0.43 ± 0.12	4.23 ± 0.63	0.38 ± 0.05	4.92 ± 1.14
q_3 (10^{-3})	0.85 ± 1.43	6.55 ± 1.16	1.46 ± 0.25	8.65 ± 2.80
ψ (rad)	2.166 ± 0.166	2.099 ± 0.102	2.187 ± 0.096	2.079 ± 0.067
ρ (10^{-3})	2.41 ± 0.04	2.40 ± 0.04	2.40 ± 0.04	2.40 ± 0.04

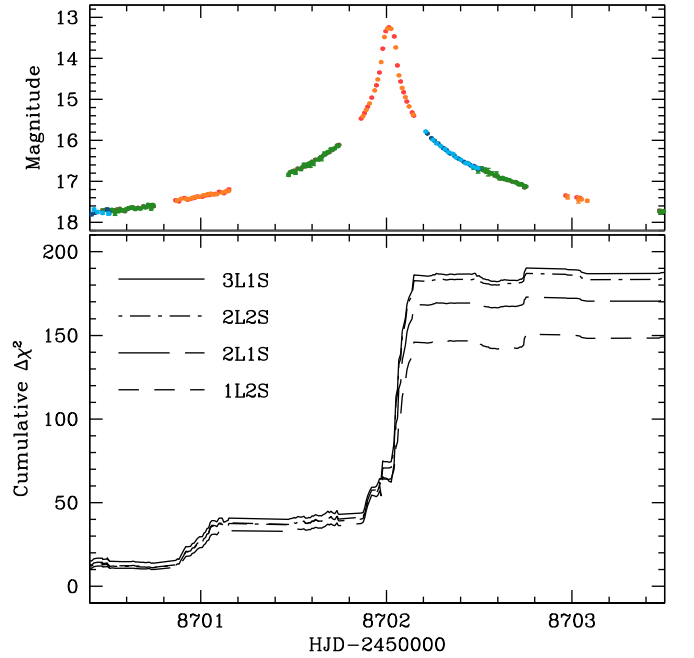**Note.** HJD′ ≡ HJD − 2450000.
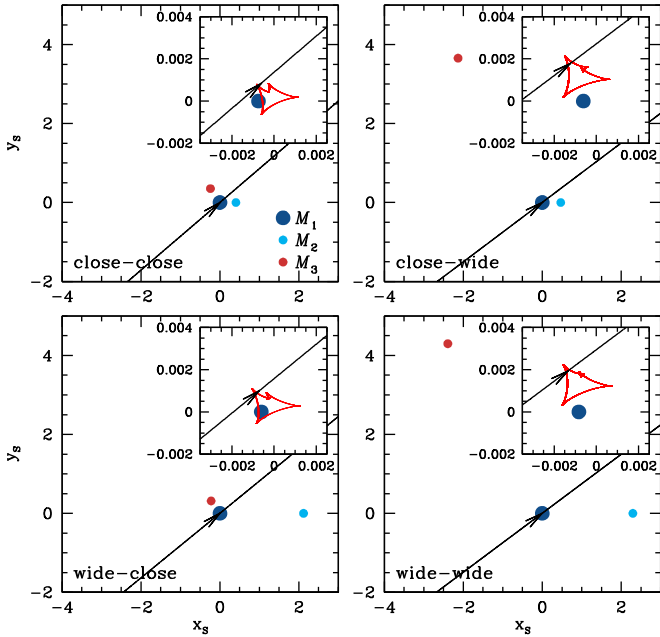
Figure 6. Lens system configurations of the four degenerate 3L1S solutions. The inset in each panel shows the zoomed-in view of the central magnification region.

Figure 7. Cumulative distributions of $\Delta\chi^2$ between the tested models (2L1S, 2L2S, and 3L1S models) and the 1L1S model. In the upper panel, the observed light curve is presented to show the region of fit improvement.

panel. For the comparison of the lens system configuration with that of the 2L2S solution, we separately present the configuration of the wide–wide 3L1S solution in the upper panel of Figure 4. From the comparison, it is found that the right parts of the caustics of the two solutions are similar to each other, but the caustic of the 3L1S solution is elongated toward the direction of M_3. For the 3L1S model, the deviations from the 2L1S model at around t_1 and t_2 are explained by the source crossing over the tip of the elongated caustic produced by M_3. For the 2L2S model, on the other hand, the deviations are explained by the second source's approach close to the caustic.

3.5. Comparison of Models

In Figure 7, we present the cumulative distributions of $\Delta\chi^2$ values of the tested models with respect to the 1L1S model. Results from the comparison of the models are summarized as follows.

1. Although the 1L1S solution approximately describes the light curve, the model leaves small but obvious deviations in the peak region.
2. The 2L1S solution with a planetary-mass companion substantially improves the fit, by $\Delta\chi^2 = 181.8$ with respect to the 1L1S solution. The 1L2S solution also improves the fit, but the model is worse than the 2L1S model by $\Delta\chi^2 = 21.3$.
3. With the 3L1S and 2L2S models, the residuals from the 2L1S solution further diminish, and the fits improve by $\Delta\chi^2 = 16.0$ and 13.5 with respect to the 2L1S model, respectively. The degeneracy between the 3L1S and 2L2S models is very severe with $\Delta\chi^2 = \chi^2_{2L2S} - \chi^2_{3L1S} = 2.5$, indicating that it is difficult to distinguish the two models based on only the light curve.

Considering the substantial improvement of the fit by the 2L1S model (single-planet model) with respect to the 1L1S model, by $\Delta\chi^2 = 181.8$, the signature of one planet is firmly

detected. However, there are two remaining issues in the interpretation of the event. The first issue is that whether the further improvement of the fit from the 2L1S model with the introduction of an extra lens component (second planet), with $\Delta\chi^2 = 16.0$, or an extra source, with $\Delta\chi^2 = 13.5$, should be seriously considered. If the signal from the extra lens or source is real, then, the second issue is which model, among the 2L2S and 3L1S models, is a correct one for the interpretation of the event.

The first issue is closely related to the threshold of detection. Dong et al. (2009) proposed $\Delta\chi^2 \sim 60$ as a threshold (and $\Delta\chi^2 \sim 150$ as a more conservative threshold) for the detection of planets through the central perturbations. Then, although the signal of the first planet, with $\Delta\chi^2 = 181.8$, is firmly detected according to this criterion, the signal of the second planet or the source companion does not meet this criterion, not even considering the increased degrees of freedom. Therefore, it is impossible to claim the 3L1S or 2L2S model for the interpretation of the event considering the unknown systematics in the data.

If the extra deviations from the 2L1S model, although weak, are real, we judge that the 3L1S model provides a more plausible interpretation of the event than the 2L2S model for two major reasons. First, the signature of the second planet according to the 3L1S solution appears in the region where it is expected, i.e., around the peak of a very highly magnified lensing event. While this is not really a reason to prefer the 3L1S model, if the opposite were true, i.e., the signal from the second planet were coming from somewhere other than the peak, it might be a reason to discount the 3L1S model. The more compelling reason to prefer the 3L1S model is that the 2L2S model is physically implausible. According to the 2L2S model, the projected separation (normalized to θ_E) between the binary source components during the lensing magnification is

$$\Delta u = \left[(u_0 - u_{0,1})^2 + \left(\frac{t_0 - t_{0,2}}{t_E} \right)^2 \right]^{1/2} \sim 0.0018. \quad (1)$$

This corresponds to the physical separation of

$$d_{S,\perp} = \Delta u D_S \theta_E \sim 0.0036 \text{ au}, \quad (2)$$

where $D_S \sim 8 \text{ kpc}$ denotes the approximate distance to the source and we use $\theta_E = 0.25 \text{ mas}$. See Section 4 for the θ_E measurement. The separation is too close for a binary system to be stable, and thus the second source would have to be projected a considerable distance in front of or behind the first source star in order to avoid merging of the two source stars. Even if the source companion is a bit further away, it would give rise to ellipsoidal variation (Han & Chang 2006) and xallarap effects (Rahvar & Dominik 2009), but such variations are not seen in the light curve. For example, if the orbital radius is three times of the projected separation, i.e., $a \sim 3d_{S,\perp} \sim 0.01 \text{ au}$ and assuming $\sim 1 M_\odot$ of the binary source, the orbital period would be

$$T = \left[\frac{(a/\text{au})^3}{M/M_\odot} \right]^{1/2} \sim 0.37 \text{ days}. \quad (3)$$

Then, there would be substantial oscillation in the lensing light curve caused by the ellipsoidal variations and xallarap effects. The data quality is good enough to see these variations, if existent,
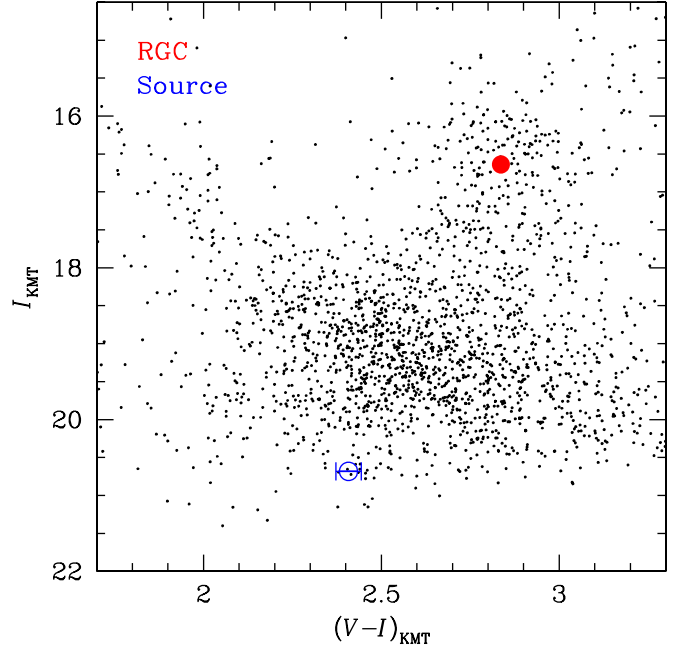
Figure 8. Source location in the instrumental color–magnitude diagram constructed using the pyDIA photometry of KMTA *I*- and *V*-band data sets. The red dot indicates the centroid of the red giant clump (RGC).

during about 10 days around the peak. Therefore, such solutions require extreme projection, and thus they are implausible.

4. Angular Einstein Radius

We estimate the angular Einstein radius from the combination of the normalized source radius ρ and the angular source radius θ_* by

$$\theta_E = \frac{\theta_*}{\rho}. \quad (4)$$

The value of ρ is measured by modeling the peak part of the light curve that is affected by finite-source effects. For the measurement of θ_E, then it is required to estimate θ_*.

We estimate the angular source radius based on the dereddened color $(V - I)_0$ and magnitude I_0 using the method of Yoo et al. (2004). Following the method, we first locate the source in the instrumental (uncalibrated) color–magnitude diagram (CMD) and then calibrate the color and magnitude using the known values of the red giant clump (RGC) centroid in the CMD as a reference. In Figure 8, we present the locations of the source and RGC centroid in the instrumental CMD constructed using the pyDIA photometry of the KMTA *I*- and *V*-band data sets. The instrumental color and magnitude of the source are $(V - I, I) = (2.41 \pm 0.04, 20.68 \pm 0.01)$. Using the offsets in color and magnitude, $\Delta(V - I, I)$, from those of the RGC centroid, located at $(V - I, I)_{RGC} = (2.84, 16.64)$, the dereddened color and magnitude of the source are estimated as $(V - I, I)_0 = (V - I, I)_{RGC,0} + \Delta(V - I, I) = (0.63 \pm 0.04, 18.39 \pm 0.01)$, where $(V - I, I)_{RGC,0} = (1.06, 14.35)$ are the known values of the dereddened color and magnitude of the RGC centroid (Bensby et al. 2013; Nataf et al. 2013). The estimated color and magnitude indicate that the source is a very late F-type main-sequence star.

With the measured $(V - I)_0$ and I_0, the angular radius of the source is estimated first by converting $V - I$ into $V - K$ using

Table 3
Angular Source Radius, Angular Einstein Radius, and Relative Lens-source Proper Motion

Quantity	Value
θ_* (μas)	0.61 ± 0.05
θ_E (mas)	0.25 ± 0.02
μ (mas yr^{-1})	5.70 ± 0.46

Note. θ_*: angular source radius, θ_E: angular Einstein radius, μ: relative lens-source proper motion.

the color–color relation of Bessell & Brett ([1988](#)) and then using the $(V - K)/\theta_*$ relation of Kervella et al. ([2004](#)). This procedure yields the angular source radius of

$$\theta_* = 0.61 \pm 0.05 \ \mu as. \tag{5}$$

With the normalized source radius, the angular Einstein radius is estimated as

$$\theta_E = 0.25 \pm 0.02 \ mas. \tag{6}$$

Together with the measured event timescale t_E, the relative lens-source proper motion is estimated as

$$\mu = \frac{\theta_E}{t_E} = 5.70 \pm 0.46 \ mas \ yr^{-1}. \tag{7}$$

To be noted is that the measured relative lens-source proper motion is similar to those of typical lensing events produced by either bulge or disk lenses that magnify background bulge source stars. In Table 3, we summarize the values of θ_*, θ_E, and μ. We note that the values of θ_E and μ are estimated based on the parameters of the 2L1S solution, because the second planet according to the 3L1S solution is not firmly detected although the solution provides a slightly better fit.

5. Physical Lens Parameters

The mass, M, and distance, D_L, to the lens are uniquely determined by measuring the angular Einstein radius θ_E and the microlens parallax, π_E, i.e.,

$$M = \frac{\theta_E}{\kappa \pi_E}; \qquad d_L = \frac{au}{\pi_E \theta_E + \pi_S}. \tag{8}$$

Here $\kappa = 4G/(c^2 au)$, $\pi_S = au/D_S$ denotes the parallax of the source, and D_S indicates the distance to the source. For KMT-2019-BLG-1953, θ_E is well measured, but the short duration of the event makes it difficult to measure π_E by the usual method of detecting light curve deviations caused by the orbital motion of Earth: annual microlens parallax (Gould [1992](#)). The KMTNet alert (August 5) was issued one week after the final upload (July 29) of the "Space-Based Microlens Parallax Survey" conducted using the Spitzer telescope (Yee et al. [2015](#)), and thus π_E could not be measured through the space-based parallax channel (Refsdal [1966](#); Gould [1994b](#)). Such high-magnification events can in principle yield terrestrial parallax measurements (Gould [1997](#); Gould et al. [2009](#); Yee et al. [2009](#)), but this generally requires that they should be observed near peak from two well-separated observatories. However, the peak of KMT-2019-BLG-1953 was only observed from KMTA, and thus π_E could not be securely measured through the terrestrial parallax channel. Not being able to determine π_E, we estimate the mass and location of the lens by conducting a
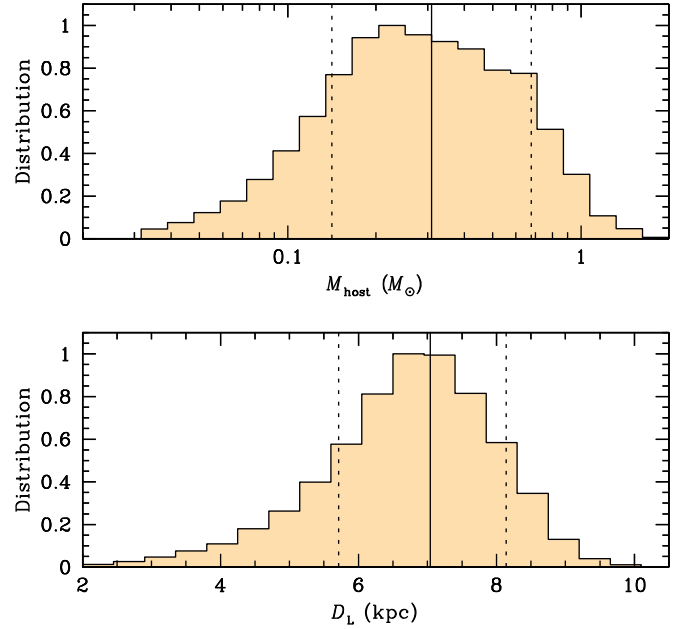
Figure 9. Probability distributions of the mass of the planet host, M_{host} (upper panel), and the distance to the lens, D_L (lower panel). The solid line in each panel indicates the median value, and the dotted lines represent the 1σ range of the distribution.

Bayesian analysis based on the measured t_E and θ_E and using the prior models of the mass function and the physical and dynamical distributions of lens objects.

For the prior distributions, we adopt the Han & Gould ([2003](#)) model for the physical lens distribution and the non-rotating barred bulge model of Han & Gould ([1995](#)) for the model of the relative lens-source motion. For the mass function, we adopt the Chabrier ([2003](#)) model for stellar lenses and Gould ([2000](#)) model for remnant lenses, i.e., white dwarfs, neutron stars, and black holes. With these prior distributions, we produce 4×10^7 artificial events by conducting a Monte Carlo simulation. We then construct the probability distribution of the physical lens parameters for events with t_E's and θ_E's located within the ranges of the measured values.

In Figure 9, we present the probability distributions for the mass of the planet host, $M_{host} \equiv M_1$ (upper panel), and the distance to the lens, D_L (lower panel). It is estimated that the host star has a mass of

$$M_{host} = 0.31^{+0.37}_{-0.17} \ M_\odot, \tag{9}$$

and is located at a distance of

$$D_L = 7.04^{+1.10}_{-1.33} \ kpc. \tag{10}$$

Therefore, the host of the planets is a low-mass star located either in the bulge or just in front of it in the disk. The mass of the confirmed planet is

$$M_p = 0.64^{+0.76}_{-0.35} \ M_J. \tag{11}$$

The mass of the second planet, if existent, is in the ranges of $0.1 \lesssim M_3/M_J \lesssim 1.1$ for solutions with $s_3 < 1.0$ and $1.1 \lesssim M_3/M_J \lesssim 6.1$ for solutions with $s_3 > 1.0$.

6. Discussion

Similar to the case of OGLE-2005-BLG-169Lb, for which the planet was discovered because of very dense sampling at

the peak (Gould et al. 2006), the signal of the potential second planet could have been clearly detected if the peak of the light curve had been much more densely observed by follow-up observations, although interpreting the signal might be subject to various types of degeneracy. Although KMTNet issued an alert for KMT-2019-BLG-1953 more than 24 hr before peak, with real-time updates to its web page[27] every three hours, no follow-up observations were taken. Here we call attention to the potential value of such follow-up observations in the case of this event, and by extension, to other similar events.

Despite the fact that KMT-2019-BLG-1953 lies in one of KMTNet's three highest-cadence fields, with a cadence of 15 minutes, the coverage was not dense enough to securely detect the second planet. Thus, even though the KMTNet observing strategy was originally designed to capture the shortest anomalies, due to Earth-mass planets, it is still not frequent enough to fully exploit the very rare extreme-magnification events such as KMT-2019-BLG-1953. In the era prior to the advent of KMTNet, such high-magnification and extremely high-magnification events were a major channel of planet detection, and they were observed at a much higher cadence (Gould et al. 2010).

Indeed, high-cadence observations from multiple well-separated sites led to terrestrial parallax measurements for two events, OGLE-2007-BLG-224 (Gould et al. 2009) and OGLE-2008-BLG-279 (Yee et al. 2009). In the case of KMT-2019-BLG-1953, it is far from clear that such well-separated observations of the peak would have yielded a successful terrestrial parallax measurement. For example, if $M \sim 0.3\,M_\odot$ and $D_S - D_L \sim 1$ kpc, as in our best Bayesian estimate, then $\pi_E \sim 0.085$ with a resulting projected velocity of $\tilde{v} \equiv \mathrm{au}/\pi_E t_E \rightarrow 1300\,\mathrm{km\,s^{-1}}$. Hence, the peaks as observed by two telescopes separated by 2500 km would have been displaced by at most 2 s. This would be too short to measure reliably. Nevertheless, without a parallax measurement, we do not know with certainty that the lens was not much closer, in which case it could have been measured.

The main point is that extreme microlensing events such as KMT-2019-BLG-1953 are a rich source of information, both about planets (multiplanetary systems) and microlens parallaxes. They occur only a few times per season, and they should be followed up with intensive observations, when possible, even in the current high-cadence surveys.

7. Summary and Conclusion

We analyzed a very high-magnification event KMT-2019-BLG-1953. The model based on the 1L1S interpretation with finite-source effects appeared to approximately describe the observed light curve, but the residuals from the model exhibited small but obvious deviations with $\Delta I \lesssim 0.07$ mag in the peak region. A 2L1S model revealed the existence of a planetary companion to the lens ($q \sim 2 \times 10^{-3}$) with a significant confidence level. It was found that additional modeling by introducing a second planetary lens companion or an extra source companion further reduced the residuals from the 2L1S model. However, this extra signal is not strong enough to confirm the additional lens or source companion. From the Bayesian analysis conducted based on the measured t_E and θ_E, it was estimated that the host of the planet was a low-mass star with a mass of $M_{\mathrm{host}} = 0.31^{+0.37}_{-0.17}\,M_\odot$ and the planetary system was located at a distance of $D_L = 7.04^{+1.10}_{-1.33}$ kpc toward the

Galactic center. The mass of the confirmed planet was in the range of $M_p = 0.64^{+0.76}_{-0.35}\,M_J$.

ORCID iDs

Cheongho Han ⬤ https://orcid.org/0000-0002-2641-9964
Michael D. Albrow ⬤ https://orcid.org/0000-0003-3316-4012
Sun-Ju Chung ⬤ https://orcid.org/0000-0001-6285-4528
Kyu-Ha Hwang ⬤ https://orcid.org/0000-0002-9241-4117
Yoon-Hyun Ryu ⬤ https://orcid.org/0000-0001-9823-2907
In-Gu Shin ⬤ https://orcid.org/0000-0002-4355-9838
Yossi Shvartzvald ⬤ https://orcid.org/0000-0003-1525-5041
Jennifer C. Yee ⬤ https://orcid.org/0000-0001-9481-7123
Weicheng Zang ⬤ https://orcid.org/0000-0001-6000-3463
Richard W. Pogge ⬤ https://orcid.org/0000-0003-1435-3053
Woong-Tae Kim ⬤ https://orcid.org/0000-0003-4625-229X
Richard Barry ⬤ https://orcid.org/0000-0003-4916-0892
David P. Bennett ⬤ https://orcid.org/0000-0001-8043-8413
Akihiko Fukui ⬤ https://orcid.org/0000-0002-4909-5763
Yoshitaka Itow ⬤ https://orcid.org/0000-0002-8198-1968
Iona Kondo ⬤ https://orcid.org/0000-0002-3401-1029
Naoki Koshimoto ⬤ https://orcid.org/0000-0003-2302-9562
Shota Miyazaki ⬤ https://orcid.org/0000-0001-9818-1513
Clément Ranc ⬤ https://orcid.org/0000-0003-2388-4534
Nicholas J. Rattenbury ⬤ https://orcid.org/0000-0001-5069-319X
Daisuke Suzuki ⬤ https://orcid.org/0000-0002-5843-9433

References

Alard, C., & Lupton, R. H. 1998, ApJ, 503, 325
Albrow, M. 2017, MichaelDAlbrow/pyDIA: Initial Release on Github (Version v1.0.0), Zenodo, doi:10.5281/zenodo.268049
Albrow, M., Horne, K., Bramich, D. M., et al. 2009, MNRAS, 397, 2099
An, J. H. 2005, MNRAS, 356, 1409
Beaulieu, J.-P., Bennett, D. P., Batista, V., et al. 2016, ApJ, 824, 83
Bennett, D. P., Rhie, S. H., Udalski, A., et al. 2016, AJ, 152, 125
Bensby, T., Yee, J. C., Feltzing, S., et al. 2013, A&A, 549, 147
Bessell, M. S., & Brett, J. M. 1988, PASP, 100, 1134
Bond, I. A., Abe, F., Dodd, R. J., et al. 2001, MNRAS, 327, 868
Bozza, V. 1999, A&A, 348, 311
Chabrier, G. 2003, ApJL, 586, L133
Chung, S.-J., Han, C., Park, B.-G., et al. 2005, ApJ, 630, 535
Claret, A. 2000, A&A, 363, 1081

---

[27] http://kmtnet.kasi.re.kr/ulens/kyuha/internal/2019alert/

Dominik, M. 1999, A&A, 349, 108
Dong, S., Bond, I. A., Gould, A., et al. 2009, ApJ, 698, 1826
Gaudi, B. S., Bennett, D. P., Udalski, A., et al. 2008, Sci, 319, 927
Gaudi, B. S., Naber, R. N., & Sackett, P. D. 1998, ApJL, 502, L33
Gould, A. 1992, ApJ, 392, 442
Gould, A. 1994a, ApJL, 421, L71
Gould, A. 1994b, ApJL, 421, L75
Gould, A. 1997, ApJ, 480, 188
Gould, A. 2000, ApJ, 535, 928
Gould, A., Dong, S., Gaudi, B. S., et al. 2010, ApJ, 720, 1073
Gould, A., Udalski, A., An, D., et al. 2006, ApJL, 644, L37
Gould, A., Udalski, A., Monard, B., et al. 2009, ApJL, 698, L147
Griest, K., & Safizadeh, N. 1998, ApJ, 500, 37
Han, C. 2006, ApJ, 638, 1080
Han, C., Bennett, D. P., Udalski, A., et al. 2019, AJ, 158, 114
Han, C., & Chang, H.-Y. 2006, ApJ, 645, 271
Han, C., Chang, H.-Y., An, J. H., & Chang, K. 2001, MNRAS, 328, 986
Han, C., & Gould, A. 1995, ApJ, 447, 53
Han, C., & Gould, A. 2003, ApJ, 592, 172

Han, C., Lee, C. -U., Udalski, A., et al. 2020, AJ, 159, 48
Han, C., Udalski, A., Choi, J.-Y., et al. 2013, ApJL, 762, L28
Hwang, K.-H., Choi, J.-Y., Bond, I. A., et al. 2013, ApJ, 778, 55
Kervella, P., Thévenin, F., di Folco, E., & Ségransan, D. 2004, A&A, 426, 29
Kim, D.-J., Kim, H.-W., Hwang, K.-H., et al. 2018, AJ, 155, 76
Kim, S.-L., Lee, C.-U., Park, B.-G., et al. 2016, JKAS, 49, 37
Nataf, D. M., Gould, A., Fouqué, P., et al. 2013, ApJ, 769, 88
Nemiroff, R. J., & Wickramasinghe, W. A. D. T. 1994, ApJL, 424, L21
Rahvar, S., & Dominik, M. 2009, MNRAS, 393, 1193
Refsdal, S. 1966, MNRAS, 134, 315
Ryu, Y.-H., Udalski, A., Yee, J. C., et al. 2020, AJ, submitted (arXiv:1905.08148)
Suzuki, D., Bennett, D. P., Udalski, A., et al. 2018, AJ, 155, 263
Tomaney, A. B., & Crotts, A. P. S. 1996, AJ, 112, 2872
Witt, H. J., & Mao, S. 1994, ApJ, 430, 505
Yee, J., Gould, A., Beichman, C., et al. 2015, ApJ, 810, 155
Yee, J. C., Shvartzvald, Y., Gal-Yam, A., et al. 2012, ApJ, 755, 102
Yee, J. C., Udalski, A., Sumi, T., et al. 2009, ApJ, 703, 2082
Yoo, J., DePoy, D. L., Gal-Yam, A., et al. 2004, ApJ, 603, 139